A Smoothed Particle Hydrodynamics model for droplet and film flow on smooth and rough fracture surfaces

J. Kordilla[b], A. Tartakovsky[1], T. Geyer[b]

[a] *Geoscientific Centre, University of Göttingen, Goldschmidstr. 3, D-37073 Göttingen, Germany.*
[b] *Computational Mathematics Group, Pacific Northwest National Laboratory, Richland, WA 99352,USA.*

Abstract

"This is the peer reviewed version of the following article: Kordilla, J., Tartakovsky, A. M., Geyer, T. (2013). Unsaturated flow, Fractured rocks, Smoothed particle hydrodynamics, Gravity-driven flow, Film flow, Surface tension. Advances in Water Resources, 59, 0309-1708., which has been published in final form at https://doi.org/10.1016/j.advwatres.2013.04.009. This article may be used for non-commercial purposes in accordance with Elsevier Terms and Conditions for Use of Self-Archived Versions."

Flow on fracture surfaces has been identified by many authors as an important flow process in unsaturated fractured rock formations. Given the complexity of flow dynamics on such small scales, robust numerical methods have to be employed in order to capture the highly dynamic interfaces and flow intermittency. In this work we use a three-dimensional multiphase Smoothed Particle Hydrodynamics (SPH) model to simulate surface tension dominated flow on smooth fracture surfaces. We model droplet and film flow over a wide range of contact angles and Reynolds numbers encountered in such flows on rock surfaces. We validate our model via comparison with

existing empirical and semi-analyical solutions for droplet flow. We use the SPH model to investigate the occurrence of adsorbed trailing films left behind droplets under various flow conditions and its importance for the flow dynamics when films and droplets coexist. It is shown that flow velocities are higher on prewetted surfaces covered by a thin film which is qualitatively attributed to the enhanced dynamic wetting and dewetting at the trailing and advancing contact lines. Finally, we demonstrate that the SPH model can be used to to study flow on rough surfaces.
Keywords:
unsaturated flow, fractured rocks, smoothed particle hydrodynamics, gravity-driven flow, film flow, surface tension

---

1. Introduction

Understanding physics of fast flow through unsaturated fractured rocks, is important for management of groundwater resources and prediction of repository performance in hard rock regions [1, 2]. The uncertainties range from process understanding at local scale to that of hydraulic understanding of regional fault zones [3]. Simulation of unsaturated flow in hard rocks represents a challenge due to highly non-linear free-surface flow dynamics and the complexity of interactions between flow in a fracture and the surrounding matrix. Hard rock formations contain fractures and other discontinuities with varying spatial parameters including orientation, density and aperture distributions [2]. Volumetric flow rates of water in unsaturated fractures may differ by several orders of magnitude from flow rates through the porous rock matrix. In sites where the rock matrix has a small permeability, fractures

may provide the primary pathways for percolation of water to the phreatic zone [4]. In this case, classical modeling approaches [5, 6] for unsaturated flow in porous media may not be accurate for flow in fractured rocks.

Recent laboratory experiments of Tokunaga and Wan [7] and Tokunaga et al. [8] have shown that film flow contributes significantly to the overall unsaturated flow in fractured rocks. Depending on the matric potential, i.e., the saturation of the matrix, films with thickness up to $70\,\mu$m and average flow velocity of $3{\cdot}10^{-7}\,$m/s may develop on fracture surfaces providing an efficient preferential pathway for laminar flow. Even faster flow velocities on fracture surfaces may develop due to the presence of droplets [9, 10], continuous rivulets [11, 12, 13, 14, 15] and falling (turbulent) films [16]. As noted by Doe [9] and Ghezzehei [16] these flow regimes may coexist with adsorbed films, however their influence on the faster flow regimes such as droplets has not been investigated by these authors and is also part of this work.

Flow rates during transitions between droplets, rivulets and falling films can range significantly in magnitude, and have been investigated by Ghezzehei [16] using an energy minimization principle. The approach is partially based on the findings of Podgorski et al. [17]. The authors investigated droplet flow on inclined surfaces and proposed a dimensionless linear scaling law to quantify flow velocities and provide a general framework and a unified dimensionless description of such flow processes. In order to apply the scaling to arbitrary fluid-substrate systems Ghezzehei [16] introduced a dimensionless scaling parameter. In this study, we employ this scaling law in a quantitative study of droplet flow on dry and wet fracture surfaces.

Given the complexity of the small-scale flow dynamics and the heterogenous nature of fractured rock surfaces, numerical models provide a significant addition to laboratory experiments and analytical solutions to investigate these systems. Models have to resolve the highly dynamic fluid interfaces as well as boundary geometries.

Traditional grid-based methods, such as Finite-Element or Volume of Fluid [18, 19] methods, in general require complex and computationally demanding interface tracking schemes. Furthermore, these methods have to rely on empirical boundary conditions specifying dynamic receding and advancing contact angles as a function of velocity. Lagrangian particle methods offer a versatile treatment of multiphase flows in domains with a complex geometry. In particle methods, there is no need for front-tracking algorithms to detect a moving interface as it moves with the particles. In addition particle methods are rigorously Galileian invariant as particle interactions only depend on relative differences in positions and velocities of the interacting particles. Furthermore, particle methods exactly conserves mass, energy and momentum due to antisymmetric particle-particle forces. Depending on the form of forces acting between particles, particle methods can model fluid flow on different spatio-temporal scales.

Molecular Dynamics (MD) is able to accurately model multiphase fluid flow on a molecular scale but modeling flow in a reasonably-sized porous domain or fracture is far out of reach of modern MD codes, even in state-of the-art High-Performance computing facilities.

Smoothed Particle Hydrodynamics (SPH, Lucy [20], Gingold and Monaghan [21]) can be seen as upscaled formulations of MD in which particles

represent fluid volumes and forces acting between particles of the same fluid phase are obtained from a meshless discetization of the Navier-Stokes equations [22]. Due to the similarity to MD, the surface tension and static and dynamic contact angles can be modeled via molecular-like pair-wise interaction forces [23]. Making these forces "soft", i.e., creating forces that have a finite magnitude for small (and zero) distances between a pair of particles, allows the SPH multiphase model to simulate flow on hydrodynamics time and length scales. A critical review of various numerical methods for multiphase flows in porous and fractured media can be found in [24]. Application of SPH for modeling flow in porous media has been demonstrated by, amongst others, Holmes et al. [25], Tartakovsky and Meakin [26], Tartakovsky et al. [27], Holmes et al. [28].

In this work we use a SPH model to study free-surface fluid flow on smooth and rough wide aperture fractures, i.e., flow bounded by a single fracture surface. This SPH model has been used before to study multiphase and free surface flows [23, 29, 30, 27], but has not been rigorously validated for three-dimensional free-surface flow dominated by capillary forces. We demonstrate that the SPH method of Tartakovsky and Meakin [23] can be applied to model dynamics of droplets on dry surfaces. Our simulations show how wetted surfaces naturally arise from droplet wetting dynamics and demonstrate the effect of prewetted surfaces on droplet flow.

The objectives of this work are: (1) the verification of the SPH model with existing empirical and semi-analytical solutions; (2) the investigation of droplet wetting behavior on initially dry surfaces for a wide range of wetting conditions; and (3) the study of transient droplet flow on fracture surfaces

covered by adsorbed films using the SPH model. To ensure numerical accuracy of the SPH simulations, the effect of resolution on static contact angles is investigated. Contact angle hysteresis for droplets in a critical state, i.e., at the verge of movement, is simulated and compared to laboratory data of ElSherbini and Jacobi [31, 32]. Transient droplet flow is verified using the dimensionless linear scaling of Podgorski et al. [17]. The formation of adsorbed films emitted from droplets on initially dry fracture surfaces and their influence on droplet flow is investigated. The effect of surface roughness on flow velocities is demonstrated.

2. Method

In the following we give a brief description of the SPH method and the governing equations. More detailed derivations and approximations involved in the SPH method can be found for example in Monaghan [33] and Tartakovsky and Meakin [23].

To derive a SPH discretization of the Navier-Stokes equations, one can start with the definition of the Dirac δ function

$$f(\boldsymbol{r}) = \int_{\Omega} f(\boldsymbol{r}')\delta(\boldsymbol{r} - \boldsymbol{r}')d\boldsymbol{r}', \tag{1}$$

where $f(\boldsymbol{r})$ is a continuous function defined on a domain Ω and $\boldsymbol{r}$ is the position vector. In SPH, for computational reasons, the δ function is replaced with a smooth, bell-shaped kernel function W [33] that produces a smoothed approximation $\langle f(\mathbf{r})\rangle$ of $f(\mathbf{r})$:

$$\langle f(\boldsymbol{r})\rangle = \int_{\Omega} f(\boldsymbol{r}')W(|\boldsymbol{r}-\boldsymbol{r}'|,h)d\boldsymbol{r}'. \tag{2}$$

For the sake of simplicity we drop the angular brackets denoting the approximation in the following. The kernel $W(|\boldsymbol{r}-\boldsymbol{r}'|,h)$ satisfies the normalization condition

$$\int_{\Omega} W(|\boldsymbol{r}-\boldsymbol{r}'|,h)d\boldsymbol{r}' = 1 \tag{3}$$

and has a compact support h such that $W(r,h) = 0$ for $r > h$. In the generalized limit of $h \to 0$, the following condition is satisfied:

$$\lim_{h\to 0} W(|\boldsymbol{r}-\boldsymbol{r}'|,h) = \delta(\boldsymbol{r}-\boldsymbol{r}'). \tag{4}$$

We use a fourth-order weighting function W [34]:

$$W(|\boldsymbol{r}|,h) = \alpha_k \begin{cases} \left(3-\frac{3|\boldsymbol{r}|}{h}\right)^5 - 6\left(2-\frac{3|\boldsymbol{r}|}{h}\right)^5 + 15\left(1-\frac{3|\boldsymbol{r}|}{h}\right)^5 & 0 \le |\boldsymbol{r}| < \frac{1}{3}\ h \\ \left(3-\frac{3|\boldsymbol{r}|}{h}\right)^5 - 6\left(2-\frac{3|\boldsymbol{r}|}{h}\right)^5 & \frac{1}{3}h \le |\boldsymbol{r}| < \frac{2}{3}\ h \\ \left(3-\frac{3|\boldsymbol{r}|}{h}\right)^5 & \frac{2}{3}h \le |\boldsymbol{r}| < \frac{2}{3}\ h \\ 0 & |\boldsymbol{r}| > h, \end{cases} \tag{5}$$

where $\alpha_k = 81/(359\pi h^3)$.

Eq. (2) can be approximated as

$$f(\boldsymbol{r}) = \sum_{j=1}^{N} f(\boldsymbol{r}_j)W(|\boldsymbol{r}-\boldsymbol{r}_j|,h)\Delta V_j, \tag{6}$$

where the domain space is discretized with a set of N particles. If $f(\mathbf{r})$ is a scalar or vector property of a fluid (e.g. fluid density or velocity), then we replace the finite volume ΔV_j by m_j/ρ_j (m_j and ρ_j are the mass and mass density of a fluid carried by particle j) and obtain a general SPH approximation for f and its gradient in terms of the values f at points $\boldsymbol{r_j}$, $f_j = f(\boldsymbol{r_j})$,

$$f(\boldsymbol{r}) = \sum_{j=1}^{N} m_j \frac{f_j}{\rho_j} W(|\boldsymbol{r} - \boldsymbol{r}_j|, h), \tag{7}$$

and

$$\boldsymbol{\nabla} f(\boldsymbol{r}) = \sum_{j=1}^{N} m_j \frac{f_j}{\rho_j} \boldsymbol{\nabla} W(|\boldsymbol{r} - \boldsymbol{r}_j|, h), \tag{8}$$

where $\boldsymbol{\nabla} W(|\boldsymbol{r} - \boldsymbol{r}_j|, h)$ is computed analytically.

Flow of each fluid phase is governed by the continuity equation,

$$\frac{d\rho}{dt} = -\rho \left(\nabla \cdot \boldsymbol{v}\right) \tag{9}$$

and the momentum conservation equation

$$\frac{d\boldsymbol{v}}{dt} = -\frac{1}{\rho}\boldsymbol{\nabla} P + \frac{\mu}{\rho}\nabla^2 \boldsymbol{v} + \boldsymbol{g}, \tag{10}$$

subject to the Young-Laplace boundary conditions at the fluid-fluid interface

$$(P_n - P_w)\mathbf{n} = (\boldsymbol{\tau}_n - \boldsymbol{\tau}_w) \cdot \mathbf{n} + S\sigma\mathbf{n} \tag{11}$$

and, under static conditions, the Young equation at the fluid-fluid-solid interface,

$$T_{nw} \cos\theta_0 + T_{sw} = T_{sn}, \tag{12}$$

where $\boldsymbol{v}$ is the volocity, $\boldsymbol{\tau} = \left[\mu(\nabla \mathbf{v} + \nabla \mathbf{v}^{\mathrm{T}})\right]$ is the viscous stress tensor, ρ is the density, μ is the viscosity, and P is the pressure of the corresponding fluid

phase. The subscripts n and w denote the non-wetting and wetting phases, correspondingly; S is the curvature of the interface and σ is the surface tension. The normal vector $\mathbf{n}$ is pointed from the non-wetting phase. The coefficients T_{nw}, T_{sw}, and T_{sn} are the specific interfacial energy between non-wetting, wetting and solid phases. The static contact angle θ_0 is a constant parameter for a given fluid-fluid-solid system. Under dynamic conditions, approximate models, such as creeping flow and lubrication flow [35], and phenomenological models [36, 37] are used to relate the contact angle to local velocities or stresses.

Using Eqs. (7) and (8), the Navier-Stokes Eqs. (9) and (10) subject to the boundary conditions (11) and (12) can be discretized as [38, 39, 23]:

$$\begin{aligned} \frac{d\boldsymbol{v}_i}{dt} &= -\sum_{j=1}^{N} m_j \left(\frac{P_j}{\rho_j^2} + \frac{P_i}{\rho_i^2}\right) \frac{\mathbf{r}_{ij}}{r_{ij}} \frac{dW(r_{ij},h)}{dr_{ij}} \\ &+ 2\mu \sum_{j=1}^{N} m_j \frac{\boldsymbol{v}_{ij}}{\rho_i \rho_j r_{ij}} \frac{dW(r_{ij},h)}{dr_{ij}} + \boldsymbol{g}_{sph} + \frac{1}{m_i} \sum_{j=1}^{N} \boldsymbol{F}_{ij}, \end{aligned} \tag{13}$$

and

$$\frac{d\boldsymbol{r}_i}{dt} = \boldsymbol{v}_i, \tag{14}$$

where $\boldsymbol{v}_i$ is the particle velocity, t is the time, P_i and μ are the fluid pressure and viscosity at $\boldsymbol{r}_i$, $r_{ij} = |\boldsymbol{r}_{ij}|$, $\boldsymbol{r}_{ij} = \boldsymbol{r}_i - \boldsymbol{r}_j$, and $\boldsymbol{v}_{ij} = \boldsymbol{v}_i - \boldsymbol{v}_j$.

For computational efficiency we set h and the mass of the SPH particles m_i to unity. A common link-list approach with an underlying square-lattice of size h is used to rapidly locate all particles within the interaction range h. All variables in the SPH model are given in consistent model units. Particle-particle interaction forces $\boldsymbol{F}_{ij}$ are added to the SPH momentum conservation

equations to generate surface tension [23]. The exact form of this force is not very important as long as it is anti-symmetric and short range repulsive, long range attractive, and is zero for a distance between particles i and j greater than h. In this work we construct $\boldsymbol{F}_{ij}$ following Liu et al. [40] who employed this type of interaction force in DPD models. The function consists of two superposed kernel functions $W_1(r_{ij}) = W(r_{ij}, h_1)$ and $W_2(r_{ij}) = W(r_{ij}, h_2)$,

$$\boldsymbol{F}_{ij} = \begin{cases} s\left(AW_1(r_{ij}, h_1)\frac{\boldsymbol{r}_{ij}}{r_{ij}} + BW_2(r_{ij}, h_2)\frac{\boldsymbol{r}_{ij}}{r_{ij}}\right) & r_{ij} \leq h \\ \\ 0 & r_{ij} > h, \end{cases} \tag{15}$$

where $A = 2.0$, $h_1 = 0.8$, $B = -1.0$ and $h_2 = 1.0$. The resulting force is smooth and continuous with short-range repulsive and long-range attractive parts as seen in Fig. 1. The parameter s controls the interaction strength and has values s_{sf} (solid-fluid) and s_{ff} (fluid-fluid). Other forms of the interaction force have been used for example by Tartakovsky and Meakin [23] who employed a cosine function. Regardless of the specific form of $\boldsymbol{F}_{ij}$, the combined effect of the pair-wise forces on any particle away from the fluid/fluid interface is near zero. Small deviations from the zero could be caused by deviations from Within the distance h from the interface, $\boldsymbol{F}_{ij}$ generates a total force acting on particles in the direction normal to the interface. In such, the SPH model is similar to the Continuous Surface Force method [41] for solving the Navier-Stokes equations subject to the Young-Laplace boundary condition at the fluid-fluid interface.

The density ρ can be obtained from the general field approximation (Eq. 7) with $f_j = \rho_j$ as,

$$\rho_i = \sum_{j=1}^{N} m_j W(\boldsymbol{r}_i - \boldsymbol{r}_j, h). \tag{16}$$

The system of SPH equations is finally closed by a van der Waals equation of state:

$$P = \frac{\rho(k_b T/m)}{1-\rho(b/m)} - \frac{a}{m}\rho^2, \tag{17}$$

where k_b is the Boltzmann constant, m is the mass of an SPH particle, T is the temperature and a and b are the van der Waals constants. Values for the constants are $k_b T = 1.6$, $a = 3.0$ and $b = 1/3$.

The SPH Eqs. (13) and (14) are integrated using a "velocity-Verlet" time stepping algorithm [42]:

$$\boldsymbol{r}_i(t+\Delta t) = \boldsymbol{r}_i(t) + \Delta t \boldsymbol{v}_i(t) + 0.5\Delta t^2 \boldsymbol{a}_i(t) \tag{18}$$

$$\boldsymbol{v}_i(t+\Delta t) = \boldsymbol{v}_i(t) + 0.5\Delta t \left[\boldsymbol{a}_i(t) + \boldsymbol{a}_i(t+\Delta t)\right]. \tag{19}$$

At each time step the density is evaluated using Eq. (16), the pressure is obtained from Eq. (17) and finally the acceleration is calculated from Eq. (13). Stability of the solution is ensured by the following time step constraints [23]:

$$\Delta t \leq 0.25 \min_i \left(\frac{h}{3|\boldsymbol{v}_i|} \right) \tag{20}$$

$$\Delta t \leq 0.25 \min_i \left(\sqrt{\frac{h}{3|\boldsymbol{a}_i|}} \right) \tag{21}$$

$$\Delta t \leq \min_i \left(\frac{\rho_i h^2}{9\mu} \right), \tag{22}$$

where $|\cdot|$ is the magnitude of a vector.

The model is initialized by placing particles randomly inside the simulation domain until the desired number density is reached. The random particle positions may lead to spurious velocities and noisy results. To avoid this, the model is equilibrated by evolving particle positions according to Eqs. (18 – 19) with $s_{ij} = 0$ and $\boldsymbol{g}_{sph} = 0$, subject to periodic boundary conditions. A higher viscosity is used at this step for (dissipative) viscous forces to quickly dampen velocity fluctuations. In this study, we assume that the flow of the liquid phase is not affected by the gas phase and solve the Navier-Stokes equations for the liquid phase only (i.e., SPH particles are only used to discretize liquid and solid phases).

Here we model droplet flow on inclined solid surfaces that form an angle α with the horizontal direction. To simplify the implementation of the SPH model, without loss of generality, we assume that the solid surface is horizontal and the body force acts at the angle $90^\circ - \alpha$ to the horizontal direction:

$$\boldsymbol{g}_{sph} = g \begin{pmatrix} cos\left(90^\circ - \alpha \frac{\pi}{180^\circ}\right) \\ 0 \\ -sin\left(90^\circ - \alpha \frac{\pi}{180^\circ}\right) \end{pmatrix}. \tag{23}$$

The final model setup consists of identifying liquid and boundary particles and removing particles from the gas phase. The summations in Eqs. (13) and (16) are over both liquid and boundary particles within the distance h from particle i. We assign the fluid viscosity to boundary particles, with the velocity of the boundary particles being zero. The viscous interaction between liquid and boundary particles generate no-slip boundary conditions

and the repulsive components of the $\boldsymbol{F}_{ij}$ force and the force resulting from the discretization of the pressure gradient produce the no-flow boundary condition. It should be noted that solid surfaces are not shown in some figures for reasons of clarity.

3. Model Calibration

3.1. Surface Tension

In our SPH model surface tension is not prescribed explicitly. It arises from the particle interaction forces and, for given A, B, h_1 and h_2, the surface tension depends on s_{ff}. Here we set the fluid-fluid interaction parameter to $s_{ff} = 0.05$. A liquid droplet in a gas phase is simulated in zero gravity and the surface tension is obtained from the Young-Laplace law:

$$\sigma_{sph} = \frac{R_{eq}}{2}\Delta P, \tag{24}$$

where R_{eq} is the droplet radius and ΔP is a difference in pressure inside and outside of the droplet. Since we do not explicitly model the air phase, the pressure outside of the bubble is zero and ΔP is equal to the liquid pressure $\overline{P}$ inside the bubble.

It should be noted that the employed EOS results in attractive and repulsive forces (these forces are combined in the first term on the right-hand-side of Eq. (13), Tartakovsky et al. [27]), but for problems with free-surfaces the attractive forces are not strong enough to generate surface tension (e.g. to form stable fluid bubbles). The addition of the $\boldsymbol{F}_{ij}$ forces is needed to create surface tension, which generates additional pressure. A total fluid pressure

within a volume V_r with radius r_v can be found from the virial theorem as shown by Tartakovsky and Meakin [23] and Allen and Tildesley [42]:

$$\overline{P} = \frac{1}{2dV_r} \sum_i \sum_j \boldsymbol{r}_{ij} \boldsymbol{f}_{ij} = \frac{1}{8r_v^3} \sum_i \sum_j \boldsymbol{r}_{ij} \boldsymbol{f}_{ij}, \tag{25}$$

where $d = 3$ in a three-dimensional system and $\boldsymbol{f}_{ij} = m_i d\boldsymbol{v}_i/dt$. In the double summations, the first summation is over all particles within distance r_v from the center of the droplet. The second summation is over all SPH particles. Since the range of the forces $\mathbf{f}_{ij}$ is equal to h, only particles within the distance r_v+h should be considered in the second summation. To exclude the boundary effect, we set $r_v = R_{eq} - h$. Droplets are equilibrated using a higher viscosity such that droplet oscillations are quickly dampened and $\overline{P}$ can be determined. As the contribution of the viscous force to $\boldsymbol{f}_{ij}$ is zero at equilibrium conditions the resulting pressure $\overline{P}$ is independent of viscous forces and, hence, the prescribed model viscosity. Surface tension obtained from the simulations of droplets of different sizes is nearly constant as can be seen in Fig. 2. However, if droplet radii are close to h, our results deviate slightly from the Young-Laplace law due to an insufficient numerical resolution.

All simulations shown in this paper use an interaction force of $s_{ff} = 0.05$ which yields a surface tension of $\sigma_{sph} = 0.25$ (in SPH model units) that was calculated as a half of the slope of the linear part of the curve in Fig. 2.

3.2. Static Contact Angles

For given A, B, h_1, h_2 and s_{ff}, the contact angle depends on s_{fs}. Here we study numerically the dependance of the static contact angle on s_{fs} and

resolution of the SPH model. This is done by simulating the behavior of a droplet that is slowly brought into contact with a flat surface. Under static conditions, this system can be described by the dimensionless Bond number,

$$Bo = \frac{\rho g V^{2/3}}{\sigma}, \tag{26}$$

where V is the volume of a droplet. In this study we consider droplets with $Bo = 1$. This corresponds to a water droplet with a volume of $V = 20.86\,\mathrm{mm}^3$. In the simulations described in this section, the density has an average value of $\rho_{sph} = 39.2$ in the model units. The characteristic size of the droplet is in the range $V^{2/3} = 8.15 - 88.95\,h^2$, depending on the resolution. The surface tension is set to $\sigma_{sph} = 0.25$. The gravitational acceleration is adjusted to the change in volume (numerical resolution) in order to keep the Bond number constant and ranges between $\boldsymbol{g}_{sph} = 0.000782 - 0.0000717$. All parameters are given in SPH model units.

To study the dependence of the static contact angle on s_{sf}, we discretize the droplet with 20390 particles that corresponds to the characteristic size of the droplet of $V^{2/3} = 60.44\,h^2$. The simulation domain has dimensions of $x = 32\,h$, $y = 32\,h$ and $z = 16\,h$ with a layer of solid particles of thickness $1\,h$. Droplets are initially equilibrated in the absence of gravity. Gravitational acceleration and solid-fluid interaction force are then gradually increased up to the prescribed values of $\boldsymbol{g}_{sph} = 0.0001139$ and $s_{sf} = 0.05$, which corresponds to $Bo = 1.0$. We then decrease the interaction force ($s_{sf} = 0.05, 0.04, ...0.01, 0.005, 0.001$) in order to determine the dependence of the contact angle on s_{sf}. Contact angles are measured "visually" once a stationary state is reached (see Fig. 3) by determination of the three-

phase contact line and the best fitting tangent [43]. As droplets may not be perfectly axisymmetric, two orthogonal cross-sections are extracted and the mean is taken from four measurements (one on each side of a cross-section). We also fitted a third-order polynomial to the particle hull. Knowing the polynomial, the contact angle at the base of the droplet can be determined analytically. This method may be more reproducible, though depending on the discretization, it may lead to high deviations as surfaces are not perfectly smooth due to their particle nature.

In order to investigate the influence of the resolution on the static contact angle we use nine droplet radii ranging from $R_{eq} = 1.77\,h$ (902 particles) to $R_{eq} = 5.85\,h$ (77993 particles) while keeping the Bond number constant at $Bo = 1.0$. Fig. 4 shows the resulting static contact angles for each droplet discretization and all fluid-solid interaction forces. Contact angles of droplets with higher resolution are closer to the mean values, however, as there is no systematic deviation from the mean at lower resolutions we conclude that the scatter of data is only a result of the measurement and not of numerical origin. Fig. 5 shows the static contact angles for each strength of the interaction force s_{sf} and the standard deviation. Simulations are restricted to static contact angles between about 110° and 25° corresponding to $s_{sf} = 0.01$ and $s_{sf} = 0.05$.

It should be noted that for very high values of the solid-fluid interaction force ($s_{sf} > 0.05$, i.e., very low contact angles) the droplet wedges may not be adequately resolved depending on the chosen discretization leading to an improper macroscopic appearance of contact angles.

4. Verification of Droplet Flow on Dry Surfaces

Transient droplet dynamics on surfaces have been investigated by numerous authors using laboratory experiments [44, 45, 17, 31, 32], theoretical methods [46, 47], and numerical models [48, 49, 50]. In the following, we show that our model agrees with empirical and semi-analytical solutions and thus can be consistently calibrated for a wide range of fluid-substrate configurations.

4.1. Critical Contact Angles

Here we investigate droplets in a critical state, i.e., at the onset of a sliding motion on an inclined plate.

Under dynamic conditions, two contact angles can be identified: the advancing contact angle θ_A, the contact angle at the drop front perpendicular to the direction of motion; and the receding contact angle θ_R, the contact angle at the drop's rear.

The dynamic contact angles at a critical state have been studied by, amongst others, ElSherbini and Jacobi [31, 32]. Their results suggest that droplets on the verge of sliding exhibit a general relation between contact angles and Bond number independent of the static contact angle. ElSherbini and Jacobi [31] examined the dynamic contact angles around the perimeter of the drop and showed that at the critical state the maximum angle θ_{max} is equal to the advancing contact angle ($\theta_{max} \approx \theta_A$) and the minimum angle θ_{min} is equal to the receding contact angle ($\theta_{min} \approx \theta_R$) for all investigated fluid-substrate combinations and Bond numbers ranging from 0.0 to 3.0. These findings are in accordance with results of Macdougall and Ockrent [51] and Tsukada et al. [52]. Here the Bond number is defined as

$$Bo' = \frac{\rho g (2R)^2}{\sigma} \sin(\alpha), \tag{27}$$

where α is the inclination angle of the surface measured from the horizontal. Based on laboratory experiments ElSherbini and Jacobi [31, 32] proposed a general non-linear (quadratic) relation between $\theta_{min}/\theta_{max}$ and Bo':

$$\frac{\theta_{min}}{\theta_{max}} = 0.01 Bo'^2 - 0.155 Bo' + 0.97. \tag{28}$$

For the numerical experiment we use several fluid-substrate configurations by varying static contact angles. This is done by varying s_{sf} from 0.0 to 0.05. In these simulations, the drop sizes range from $R_{eq} = 1.77$ to 5.85, resulting in $Bo' = 0.14 - 2.8$. Gravitational acceleration is set to $\boldsymbol{g}_{sph} = 0.000164$, average density is $\rho_{sph} = 39.2$ and surface tension $\sigma_{sph} = 0.25$.

Similar to the determination of static contact angles, the droplets are equilibrated by setting $\boldsymbol{g}_{sph} = 0.0$ and then slowly placed on a horizontal surface by increasing the gravitational acceleration. When the height of the droplets becomes constant (the droplets reached an equilibrium on a flat surface), we start increasing the surface inclination by one degree every 150 time steps giving the drop enough time to adjust. The receding and advancing contact angle are measured when droplet movement of the receding and advancing contact line sets on, i.e., at the critical state. Fig. 6 shows a droplet with radius $R_{eq} = 4.82\,h$ and four different static contact angles between 60° and 110° ($s_{sf} = 0.01, 0.02, 0.025, 0.03$) in its critical state.

Our results are in a good agreement with the findings of ElSherbini and Jacobi [31] as shown in Fig. 7. Most of our numerical results are within the margin of error of the experimental measurements in ElSherbini and

Jacobi [31]. A slight deviation can be observed for very high Bond numbers above 2.0. We believe that this may be a result of: (1) the error introduced when measuring the contact angles in our simulations; and (2) an insufficient discretization of the droplet wedges at low contact angles (i.e., high solid-fluid interaction forces) that are necessary to achieve a critical state at such high inclination angles (i.e., Bond numbers).

4.2. Dimensionless Scaling

Transient droplet flow on subhorizontal surfaces can be extremely complex. However, as shown by Podgorski et al. [17] a general scaling law can be applied in order to quantify droplet flow dynamics within a certain range of conditions. Based on laboratory experiments using silicon oils and deionized water as well as several substrates, Podgorski et al. [17] proposed a linear scaling law that relies on a force balance:

$$Ca \sim Bo \sin(\alpha) - \Delta_\theta, \tag{29}$$

where the capillary number is defined as

$$Ca = \mu v / \sigma, \tag{30}$$

with v being the droplet velocity, α is the surface inclination angle measured from the horizontal and Δ_θ is a perimeter-averaged projection factor of the surface tension. In order to apply the scaling to various static contact angles in our numerical experiments, we follow Ghezzehei [16] to define a proportionality constant γ such that Eq. (29) becomes

$$Ca = \gamma \; Bo \sin(\alpha) - \Delta_\theta \tag{31}$$

and γ and Δ_θ can be determined as empirical constants unique for a given static contact angle.

The model domain used for transient droplet flow has dimensions $x = 128\,h$, $y = 64\,h$ and $z = 16\,h$ which corresponds to $45.7\,\mathrm{x}\,22.8\,\mathrm{x}\,5.7\,\mathrm{mm}$ in SI units. Periodic boundary conditions are used in the x- and y-directions.

The model is set up analogous to a typical laboratory experiment for measurements of contact angles. After a droplet equilibrates on a surface with prescribed inclination for the desired interaction force ($s_{sf} = 0.01, 0.02...0.05$), gravitational acceleration is gradually increased until the prescribed value of $\boldsymbol{g}_{sph} = 0.0001139$ is reached.

Bond number in the simulations range from 0.14 to 1.5, with the droplet radii ranging between $1.77\,h$ and $5.85\,h$ or 0.63 and 2.09 mm. Surface inclinations are held constant throughout each simulation at angles ranging from 10° to 90° measured from the horizontal. This yields a total of 81 $Bo \cdot sin(\alpha)$ values for every static contact angle θ_0. In addition we also use three different values for the viscosity ($\mu_{sph} = 0.01, 0.03, 0.1$) to cover a feasible range of Reynolds numbers observed in water-rock systems. Depending on the contact angle, obtained Reynolds numbers range from $Re = 302 - 3908$ for $\mu = 0.01$, $Re = 67 - 1299$ for $\mu = 0.03$, and $Re = 15 - 387$ for $\mu = 0.1$.

Droplet bulk velocities are measured as soon as the maximum velocity is reached. We track the droplet front position and evaluate $\Delta x/\Delta t$ where Δt is a time interval long enough to average out fluctuations in particles positions that may occur at the droplet front due to the dynamic wetting

process. This behavior can be observed at low Bond numbers when body forces only partially exceed drag forces due to the slightly non-homogeneous density distribution of the wall particles.

Fig. 8 shows simulation results for two different droplet sizes $R_{eq} = 2.8\,h$ and $4.82\,h$ ($Bo = 0.34, 1.02$) at the same time for several viscosities, static contact angles at an inclination angle of $\alpha = 90°$. Note that the maximum velocity of some droplets at very low capillary numbers (e.g. for $s_{sf} = 0.01, \theta_0 = 110°$) occurs after crossing the x-direction periodic boundary. The shown simulation snapshots are taken before the droplets crossed the boundary and droplet shapes are mainly round or slightly cornered at this (early) time such that the force balance assumptions of Podgorski et al. [17] are correct. However, depending on capillary and Bond number, the scaling law is applied only to fully accelerated droplets, which show several effects that have to be considered for the interpretation of the results.

As noted by Podgorski et al. [17] the linear scaling fails above a certain capillary number in the pearling regime when droplets develop strong tails and emit smaller static droplets via a Rayleigh-like instability. Subsequent droplets that absorb such emitted droplets may experience a drag reduction when the emitted droplet size is big enough. Consequently, γ values determined in the laboratory experiment are slightly higher in this regime and cannot be determined independent of droplet size (i.e., Bond number). Furthermore, the scaling can only be applied to droplets with a radius smaller or on the order of the capillary length λ_c of the fluid, where

$$\lambda_c = \sqrt{\frac{\sigma}{\rho g}}, \tag{32}$$

which assumes values of $R = 56\,h$ (2.75 mm at average subsurface temperatures of 10°C).

For droplets that do not strongly deviate from the rounded or cornered shape, the velocities (or Ca) obtained from the SPH simulations agree with the Podgorski scaling (see Fig. 9). However, for hydrophobic surfaces (i.e., $\theta_0 = 110°$) the velocities obtained from the SPH model deviate from the linear scaling predicted by the theory of Podgorski et al. [17]. This disagreement can be explained by the fact that a droplet on a non-wetting surface and flowing down with high velocity may develop a rolling behavior that violates the force balance assumptions in the Podgorski et al. [17] theory.

We observe top view droplet shapes ranging from round to slightly cornered and strongly elongated for high static contact angles ($s_{sf} = 0.01, 0.02$) (see Fig. 10). As a result, droplets above a certain Ca value experience a drag increase due to the higher contact area such that γ values (given by a slope of the linear part of the curves in Fig. 9) become lower (see for example the upper row, data points above dashed line). Due to the poor linear relationship in this Ca range the scaling depends on the areal extent of the droplet such that no common γ value can be determined for all simulations.

For lower static contact angles ($s_{sf} = 0.03, 0.04, 0.05$) droplets develop a trailing film of varying thickness which is only poorly developed for intermediate static contact angles ($s_{sf} = 0.03$, $\theta_0 = 60°$) as can be seen in Fig. 11. Within the simulated timespan the change in droplet mass, i.e., the ratio of fluid volume in the film and in the droplet, is negligible such that the force balance of Podgorski et al. [17] can still be applied. However, for longer simulations it is clear that droplet movement will slow down and

finally stop when the droplet sizes are below the critical Bond number and the main fluid volume resides in the film. The formation of trailing droplets, as it has been observed by [17], is present in our simulations, however, due to their small size (relative to h) the trailing droplets are resolved by only a few SPH particles and most likely do not behave quantitatively correct. Furthermore, the pronounced pearling regime described by [17] occurs for Bond numbers above 1.5 (and static contact angles of about 50°), which we do not cover in our simulations. To our knowledge the occurrence of trailing films over such a range of wetting properties has not been quantified in laboratory experiments, therefore the influence of this on droplet flow is shown in the following section.

5. Droplet Flow on Inclined Wet Surfaces

We define a stationary moving droplet as a droplet whose mass and shape does not change as it flows down the surface. In the above section we observed that stationary moving droplets cannot be formed on a dry surface if the static contact angle is small. To study dynamics of stationary moving droplets with low static contact angles, we conduct a second set of simulations using a prewetted surface. The initial surface film thickness is determined by probing the film left behind in the simulations with initially dry conditions in order to find the appropriate average amount of particles. We assume that the thickness of trailing films in our simulations reflects the maximum fluid capacity kept as film for a given fluid-substrate combination and thus acts as a lubrification for droplets by enhancing the dynamic wetting and dewetting at the advancing and receding contact line. Furthermore, a stationary

moving droplet develops at a maximum velocity.

Even though droplets at intermediate static contact angles ($s_{sf} = 0.03$, $\theta_0 = 60°$) also leave behind partial films, it is impossible to create a prewetted surface as the initial films immediately break up via a Marangoni-like instability for $s_{sf} \leq 0.03$ (see Fig. 12). Consequently droplets will coalesce and their volume changes such that the force balance cannot be applied. Therefore we restrict the simulations with prewetted surfaces to static contact angles $\theta_0 = 25°$ and $\theta_0 = 40°$.

Fig. 13 shows droplets at maximum acceleration sliding on the prewetted surface. The film thickness varies between $0.3 - 0.5\,h$ which corresponds to $107 - 178\,\mu$m. This is higher than what has been reported for example by Tokunaga and Wan [7], Tokunaga et al. [8] ($2 - 70\,\mu$m) and Dragila and Weisbrod [10] ($0.9 - 40\,\mu$m) but of the right order of magnitude. However, as also noted by Tartakovsky and Meakin [23], depending on the chosen SPH resolution, simulations may become (1) computationally too expensive in order to cover such length scales and (2) hydrodynamics of thin adsorbed films may not be adequately represented by the Navier-Stokes approximations when chemical potentials dominate flow behavior [53, 54].

Applying the dimensionless scaling to the prewetted simulations yields a general increase of γ values with droplet velocities being nearly tripled for a viscosity of $\mu_{sph} = 0.1$ (see Fig. 14). Fig. 15 gives a comprehensive overview of the scaling parameter and shows that the velocity increase is less pronounced at lower viscosities ($\mu_{sph} = 0.01, 0.03$). Partially, this might be caused by droplets still "loosing" SPH particles to the prewetted surface, especially during the initial placement of the droplets when the gravitation

is slowly increased. We use only droplets with radii bigger than 4.31 h to determine the scaling, as smaller droplets below the critical Bond number are stuck on the surface but may still display some fluctuating movement induced by interaction with the film.

Fig. 16 shows the resulting maximum Reynolds numbers from our numerical experiments under dry and prewetted surface conditions for all tested static contact angles. Ranges for the occurrence of adsorbed films, which develop under dry surface conditions when droplets leave behind trails, are given as a function of s_{sf} and Re where

$$Re = \frac{\rho v V^{(1/3)}}{\mu}. \tag{33}$$

In general two flow regimes can be distinguished: (1) droplets without trailing films and (2) droplets with trailing films of varying thickness. The former can be observed over the whole range of the modeled viscosities with a static contact angle of $\sim$110° ($s_{sf} = 0.01$). At lower static contact angles (between 80° and $\sim$60°) only droplets with a viscosity of $\mu = 0.1$, i.e., lower Reynolds numbers, are free of trailing films. Droplets with a static contact angle smaller $\sim$80° ($s_{sf} = 0.02$) and $\mu \leq 0.03$ all leave trailing films where the film thickness is higher for lower viscosities and/or lower static contact angles. This observation can be attributed to the fact that both lower viscosity and lower static contact angle (corresponds to small ratio s_{ff}/s_{sf}) facilitate the fluid spreading along the surface.

The calculated Reynolds numbers and the range of static contact angles are in agreement with the ranges reported in literature. For example, the highest Reynolds number obtained in our simulations is of the same order

obtained in a laboratory experiment for a similar microscale system [13]. Static contact angles reported in experiments range from 23° to 70° (e.g. [55, 56, 57, 11]) and are also within the range of angles produced by our SPH model. Therefore, the presented simulation results give a comprehensive overview of the flow dynamics that could be expected under experimental and most common field conditions.

6. Droplet Flow on Rough Surfaces

Here we study the effect of surface roughness on the droplet flow. The simulation setup now consists of surfaces with a self-affine fractal geometry [58] described by the Hurst exponent ζ [59], which has a nearly constant value of about 0.8 ± 0.05 independent of the material [60, 61]. The domain size for the simulations is the same as in section 4.2. We employ three surfaces with a Hurst exponent of $\zeta = 0.75,\ 0.50,\ 0.25$ (see Fig. 17). The viscosity is set to $\mu = 0.03$ and the droplet radius is $5.85\,h$. The surface inclination is set to 90° and 45° and solid-fluid interaction forces are $s_{sf} = 0.01,\ 0.02,\ 0.03$ ($\theta_0 = 110°$, $80°\,60°$). Fig. 18 shows the resulting Reynolds numbers (i.e., dimensionless velocity) for the surfaces with different roughnesses and the smooth surface. Our results shows that surface roughnesses decreases the velocity of droplets. For $\theta_0 = 110°$ and $80°$ we observe the velocity decrease between 33% and 37% for a roughness coefficient $\zeta = 0.75$ in comparison with the smooth surface. These results are independent of the surface inclination. For $\theta_0 = 60°$, the velocity decreases by as much as 80% for an inclination angle of 90° and 98% for in inclination angle of 45°. For lower Hurst exponents, i.e., "rougher" surfaces, droplets with static contact angle of 60° barely move,

while for higher contact angles the velocity is almost linearly proportional to ζ, i.e., the velocity decreases linearly with decreasing Hurst exponent. Our simulations suggest that, for low contact angles, little pits and depressions created by the roughness cause an additional capillary suction which prevents the movement of droplets.

7. Conclusion

We employed a three-dimensional multiphase SPH model to simulate gravity-driven free-surface flow dominated by the effects of surface tension. The model uses pair-wise interaction forces to represent fluid-fluid and fluid-solid interactions and allows modeling a wide range of wetting conditions. Various flow conditions have been investigated and the model ability to simulate (1) wetting and non-wetting droplet flow on dry surfaces and (2) flow on surfaces prewetted with adsorbed films has been demonstrated.

Static contact angles of sessile droplets are shown to be independent of the chosen resolution, i.e., computation time can be saved while still preserving physically correct model behavior.

The dynamic contact angle hysteresis for droplets at the verge of movement, i.e., at the critical state, matches empirical experiments of ElSherbini and Jacobi [31]. Droplets with higher Bond numbers (that is, low static contact angles and higher inclination angles at a critical state) exhibit a slightly higher $\theta_{min}/\theta_{max}$ ratio which is believed to be a result of an insufficient resolution of droplet wedges.

In order to further verify our model for transient flow conditions we have shown that it can reproduce the linear scaling proposed by Podgorski et al.

[17]. We have demonstrated that Ca, Re, and contact angles agree with those reported in laboratory experiments for water-rock systems for a wide range of Bo. We have also shown that the SPH model can be used to estimate the scaling parameter γ as a function of the static contact angle in the model of Ghezzehei [16].

Our simulations show that the linear scaling fails as soon as droplet shapes strongly deviate from a rounded or cornered shape. This is in accordance with the observations of Podgorski et al. [17].

We found that droplets on dry surfaces leave behind trailing films for small static contact angles and initially dry surfaces. These results agree with experimental observations of Tokunaga and Wan [7] and Or and Tuller [53]. Prewetted surfaces are shown to increase droplets velocities by enhancing the wetting and dewetting dynamics processes and thus, despite their relatively slow velocities ($3{\cdot}10^{-7}$ m/s, [8]) can be an important part of flow dynamics even if gravity-driven flow prevails. Our simulations show that fluid films are stable for static contact angles below $\sim 40^{\circ}$. These results indicate that flow regime (droplets leaving behind a dry surface versus droplets leaving behind discontinuous or continuous films) and droplet velocity (Reynolds number) depend on the static contact angle and initial wetting condition of the fracture wall (dry versus prewetted). Therefore, a flow regime may affect the average flux in the fracture and should be accounted for in an effective model.

We considered the effect of "macroscale" roughness on the drop dynamics and demonstrated that it affects traveling distance and transversal movement. We define a macroscale roughness when the following conditions are

satisfied: (1) the ratio of characteristic roughness length scale d_r to average interparticle distance d_p is on the order of one or higher; and (2) the characteristic roughness length is much smaller than the capillary length λ_c. Microscale roughness (i.e., $d_r/d_p << 1$ and $d_r/\lambda_c << 1$) may result in more complex phenomena such as the lotus effect [62, 48] and apparent contact angles [63]. However, studying the effect of the microroughness is outside of the scope of this work as simulation of such phenomena would require exascale computations with the number of SPH particles on the order of 10^7 to 10^9.

The following topics deserve more attention for further model applications: (1) the critical transitions between different flow regimes, e.g. forced wetting transitions such as Landau-Levich films which occur for very low contact angles [47]; (2) shape transitions from oval to corner and cusps which involve field singularities; and (3) transitions to rivulets and falling films. Given that the application of our model is aimed towards fractured media we defined a lower scale that we believe is a proper starting point for model development and allows realistic computation times. Further model improvements might cover implementation of more realistic boundary conditions, however, for rough surfaces this is still an open question [64].

The presented simulations cover a wide spectrum of the possible flow regimes and boundary conditions encountered in natural fractured aquifers. Furthermore, these simulations demonstrate that SPH is a versatile method and can be easily extended to simulate more complex systems, allowing for a unified characterization of the flow and possibly transport processes across the matrix-fracture interface in partial fracture networks on a centimeter to

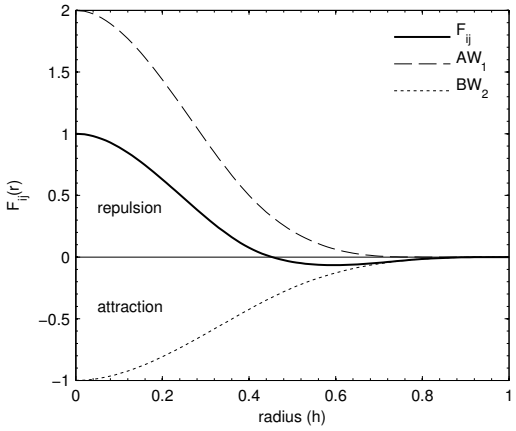

Figure 1: The interaction potential consists of two superimposed cubic spline functions W_1 and W_2 with parameters A and B following Liu et al. [40]

meter scale, which is the scope of future work.

Acknowledgments

The authors would like to thank four anonymous reviewers. This work was partially supported by the DAAD (German Academic Exchange Service) providing J. Kordilla with an international research scholarship at the Pacific Northwest National Laboratory (PNNL), USA. A.M. Tartakovsky was supported by the Department of Energy's Office of Advanced Scientific Computing Research Program and at Pacific Northwest National Laboratory (PNNL). PNNL is operated by Battelle for the U.S. Department of Energy.

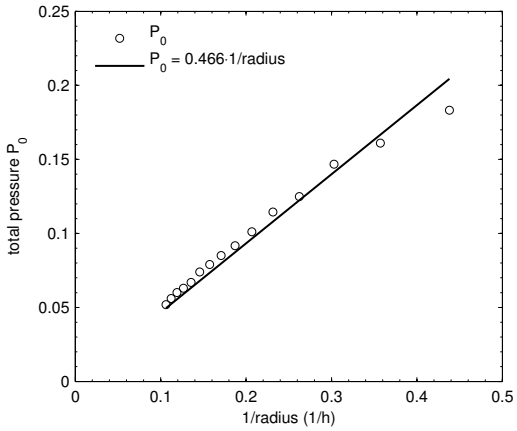

Figure 2: Surface tension and pressure for various droplet sizes, $\boldsymbol{g}_{sph} = 0$, $s_{ff} = 0.05$

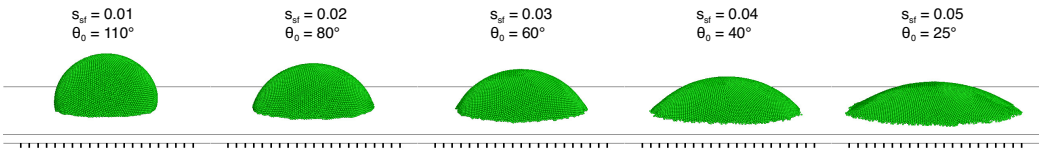

Figure 3: Static contact angles for different fluid-solid interactions strengths s_{sf}. Shown droplets have an equilibrated radius of $R_{eq} = 5.85\,\mathrm{h}$ and $Bo = 1.0$. Tick marks have 1 h spacing.

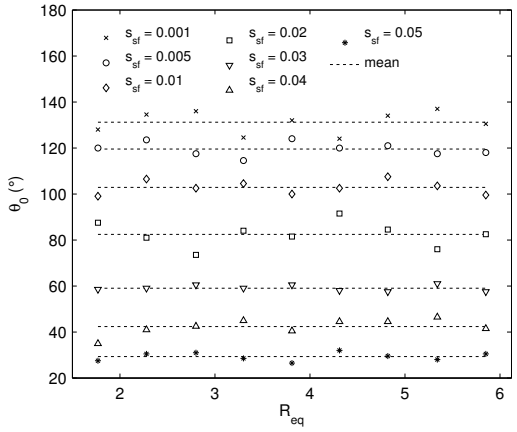

Figure 4: Static contact angles for different droplet resolutions and their mean values.

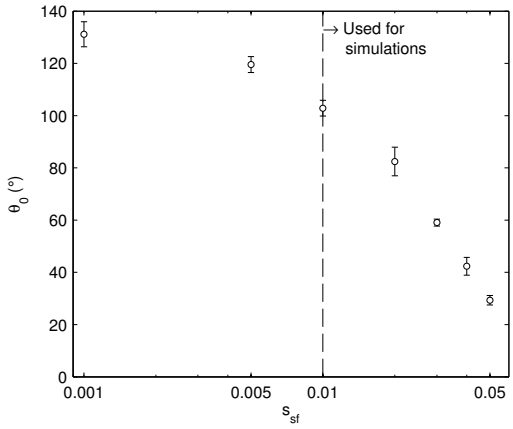

Figure 5: Mean static contact angles for varying interaction force s_{sf} and standard deviation. Bo = 1.0 for all radii.

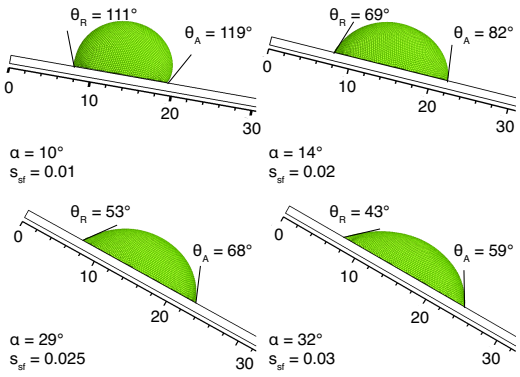

Figure 6: Advancing and receding contact angles for droplets in a critical state. All shown droplets have the same equilibrated radius of 4.82 h ($Bo = 1.02$) and static contact angles between 60° and 110°.

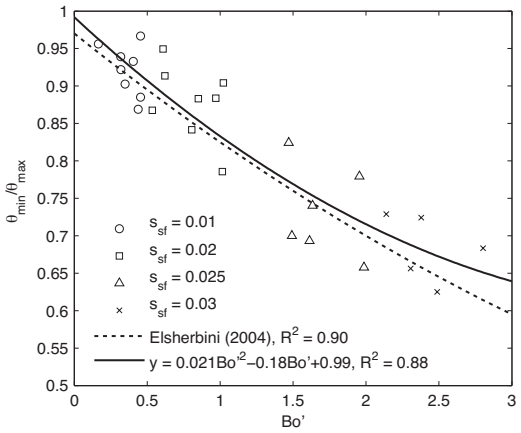

Figure 7: $\theta_{min}/\theta_{max}$ ratios for Bond numbers between 0.0 and 3.0 and several fluid-solid interaction strengths s_{sf}. Note that Bo' is defined according to Eq. (27). Contact angle measurement are estimated to yield an error of $\pm 5°$.

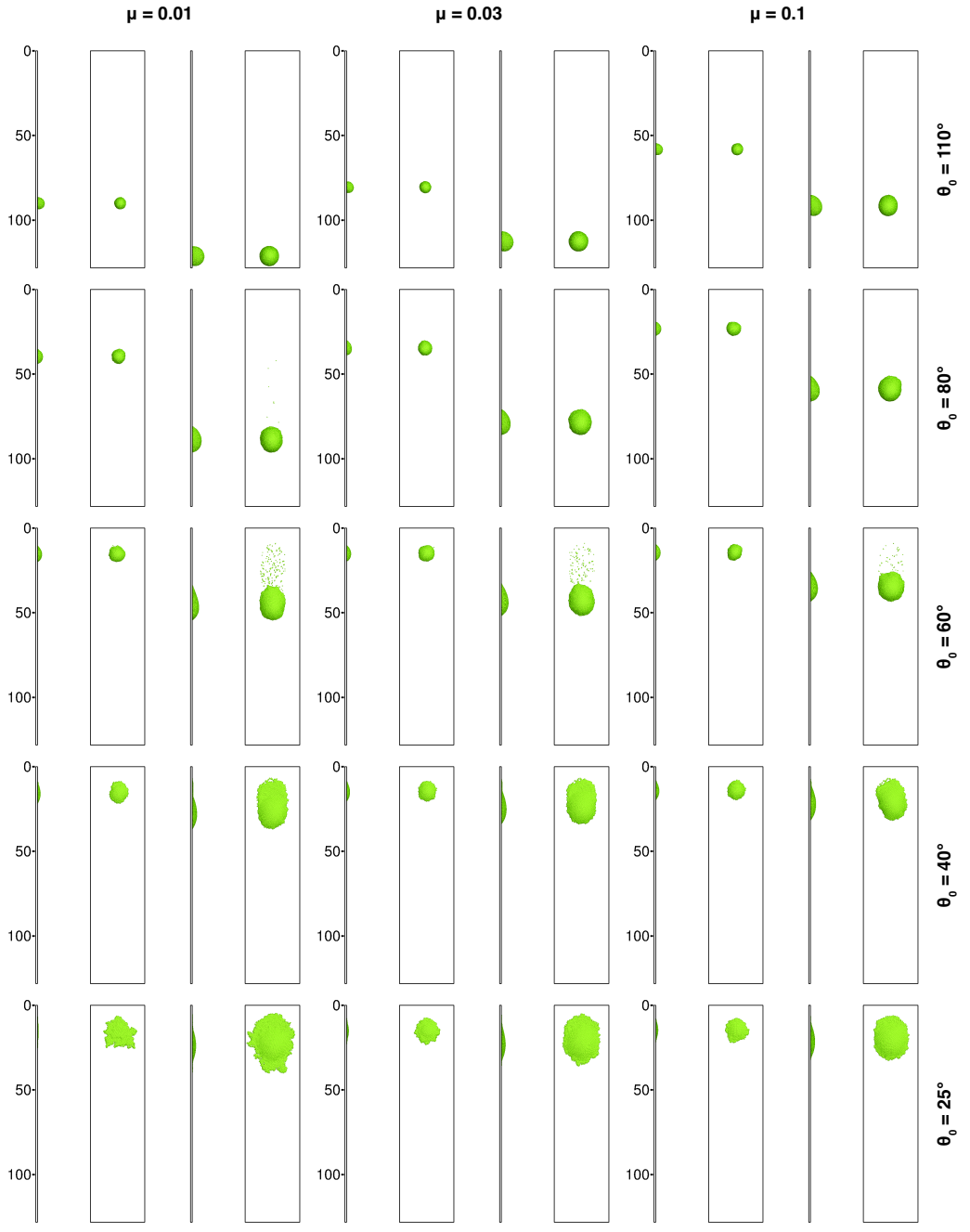

Figure 8: Simulation results for two droplet sizes ($R_{eq} = 2.28\,\mathrm{h}$ and $R_{eq} = 4.82\,\mathrm{h}$) at time step $t = 1800$ (116.25 ms) for three viscosities $\mu_{sph} = 0.01, 0.03, 0.1$ and five interaction strengths $s_{sf} = 0.01, 0.02...0.05$ (static contact angles from 25-100° at an inclination angle $\alpha = 90°$. Note that all shown droplets have not yet crossed the mirror boundary at the shown time step. At later time steps faster droplets cross the x-direction mirror boundary several times.

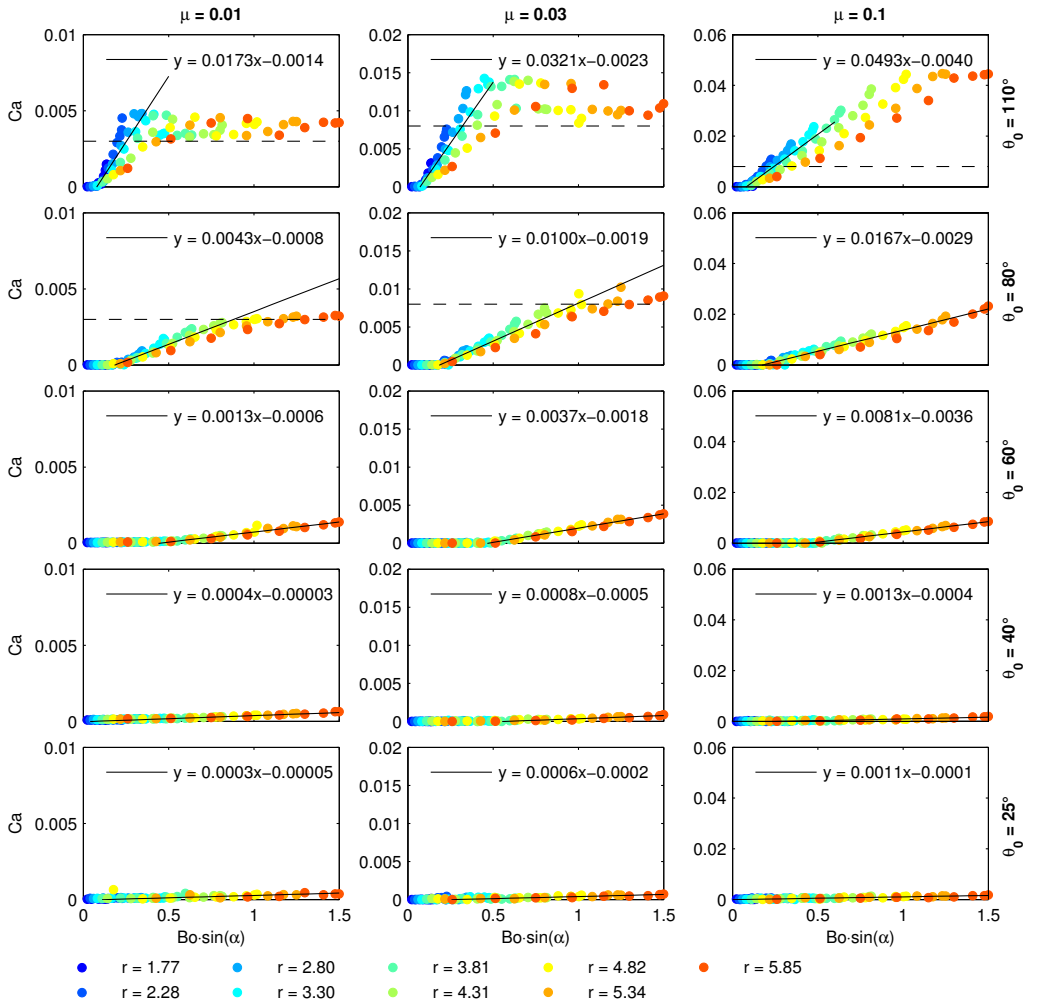

Figure 9: Dimensionless scaling according to [17] for three viscosities $\mu_{sph} = 0.01, 0.03, 0.1$, five interaction strengths $s_{sf} = 0.01, 0.02...0.05$ at several inclination angles α =25 – 100° and nine different droplet sizes (1.77 h and 5.85 h, 0.63 and 2.09 mm). Droplets above the dashed lines show a strong deviation from the rounded or spherical shape such that the linear scaling fails and are not included in the calculation of γ and Δ_θ. Below a certain Ca value scaling parameters are partially difficult to determine due to sudden particle fluctuations and droplet front movement caused by strong interactions forces.

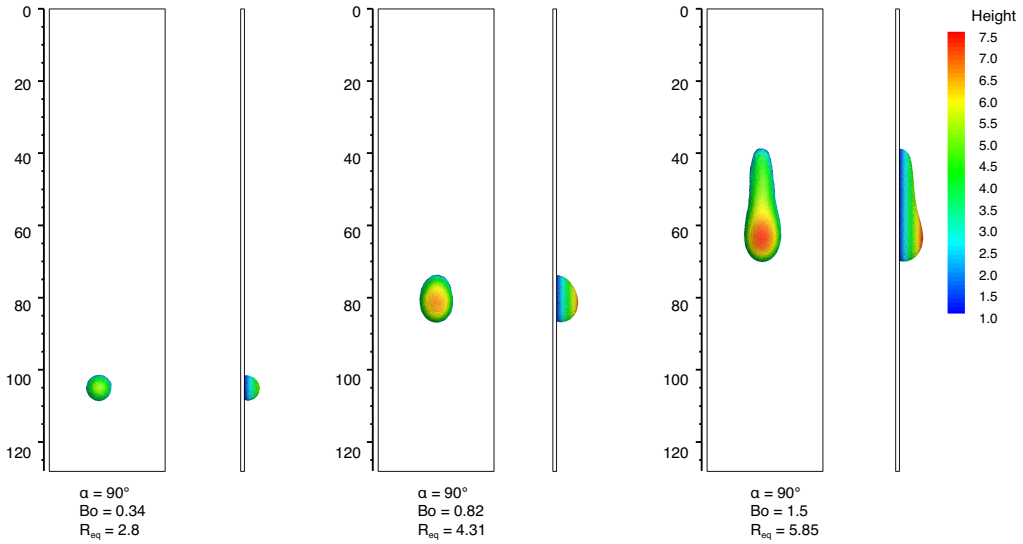

Figure 10: Depending on capillary and Bond number droplet shapes range from round (left) to slightly cornered with a strong elongation (right). Time is $t = 4800$ (0.31 s) with $\mu_{sph} = 0.03$ and $s_{sf} = 0.01$ ($\theta_0 = 110°$)

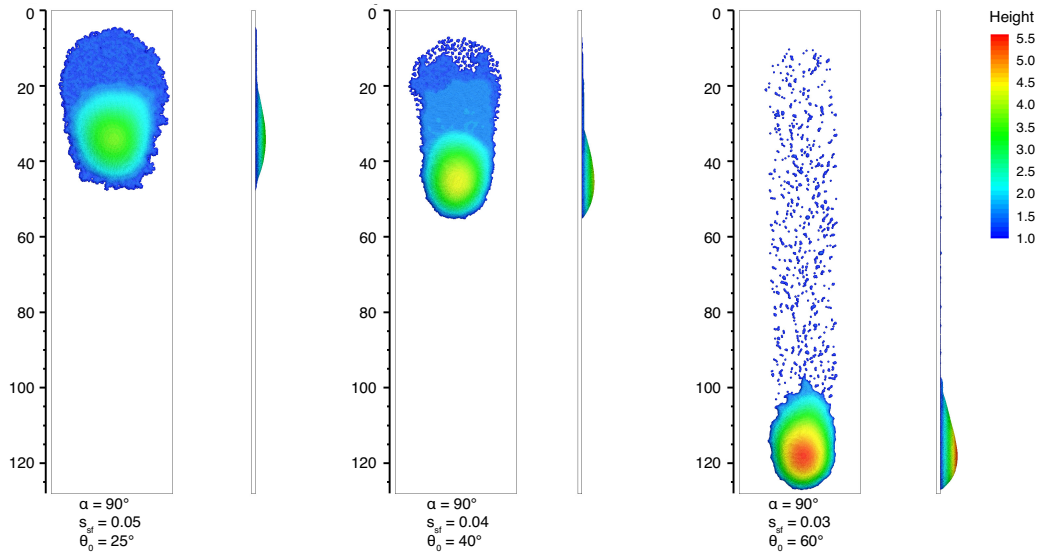

Figure 11: Trailing films of droplets with $s_{sf} = 0.05$, $s_{sf} = 0.04$ and $s_{sf} = 0.03$ (from left to right). μ_{sph} is 0.03 and $t = 4800$ (0.31 s).

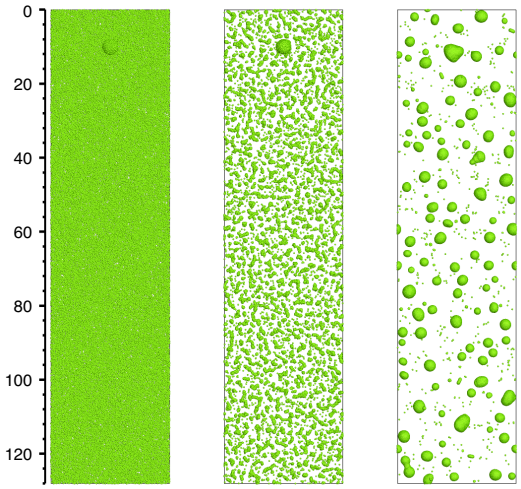

Figure 12: Prewetted surfaces with $s_{sf} \leq 0.03$ exhibit a Marangoni-like breakup of films and are not used in the simulations. Shown example has an interaction force $s_{sf} = 0.01$ with $\mu_{sph} = 0.03$ and t=1, 10, 340 (0.64 ms, 21.9 ms).

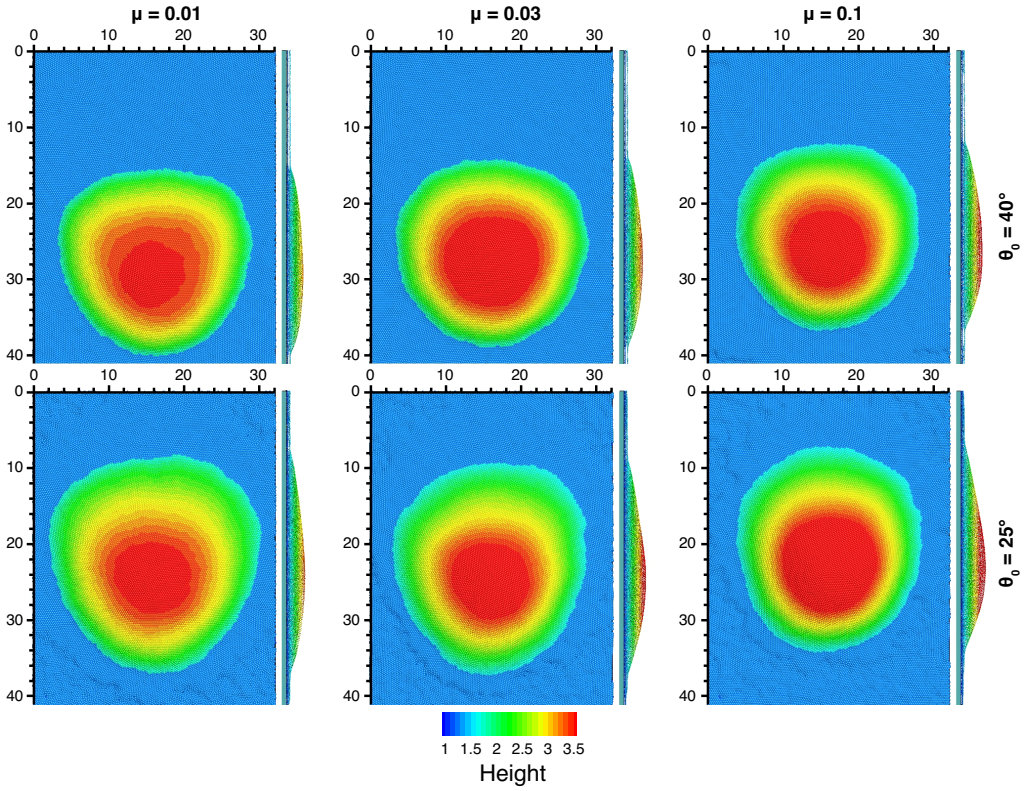

Figure 13: Droplets sliding on a prewetted surface with equilibrated radius $R_{eq} = 5.85\,\mathrm{h}$ at maximum acceleration (t=2670, 0.17 s). Maximum film thickness is about $0.3-0.5\,h$ ($107-178\,\mu$m).

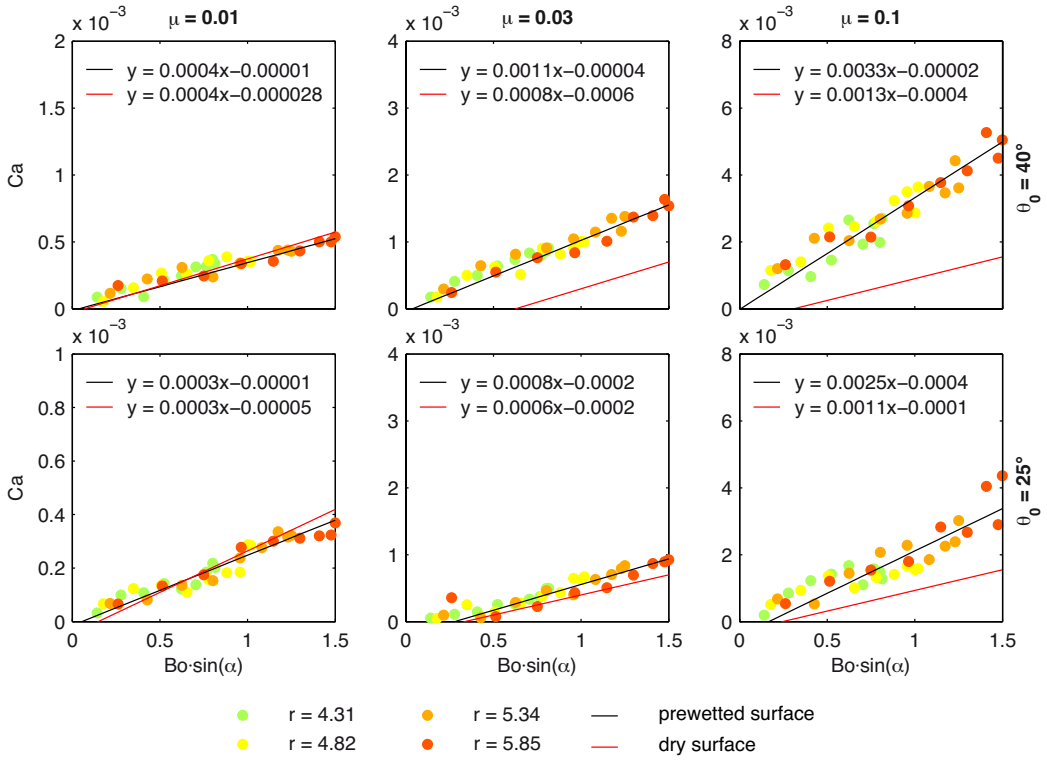

Figure 14: Dimensionless scaling for three viscosities $\mu_{sph} = 0.01, 0.03, 0.1$ and two interaction strengths $s_{sf} = 0.04$ and $s_{sf} = 0.05$ with a prewetted surface. Scaling parameter of the dry surface are shown for comparison. Note that droplets with radius $R_{eq} < 4.31\,\mathrm{h}$ are not moving but exhibit spreading effects and sudden particle fluctuations and are thus not included in the calculation.

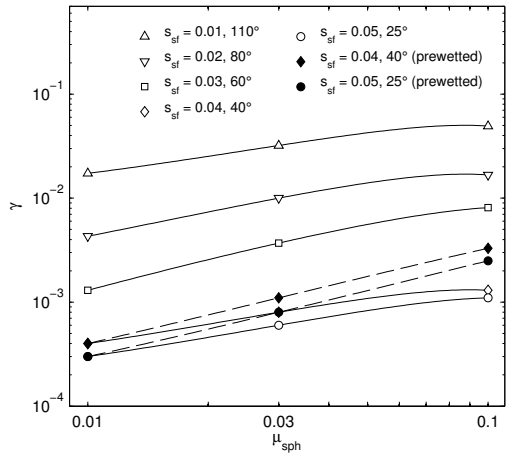

Figure 15: Scaling parameter γ as defined by Ghezzehei [16] vs. viscosity μ_{sph} for all investigated static contact angles under dry and prewetted surface conditions. Droplets on prewetted surfaces display increased velocities by a factor of up to three ($\mu_{sph} = 0.1$).

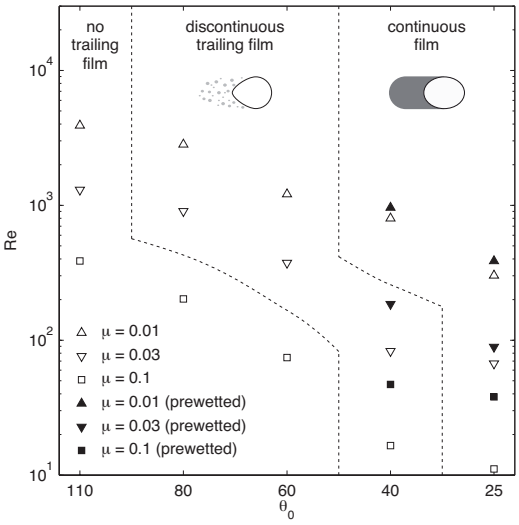

Figure 16: Maximum Reynolds numbers for all investigated static contact angles and viscosities for dry and prewetted surfaces. Trailing films vary in volume and appear more pronounced at higher Reynolds numbers and static contact angles. Regime transitions have been approximated based on simulation data.

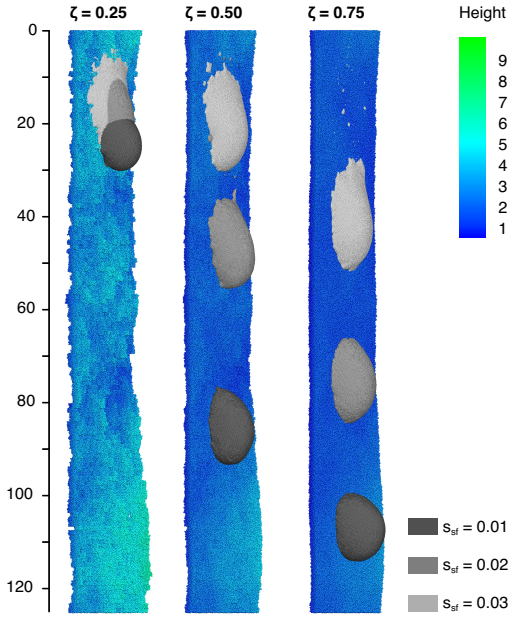

Figure 17: Advancing droplets on rough surfaces with Hurst coefficients $\zeta = 0.25$, 0.5 and 0.75 at time t=2000 (0.13 s). Results are shown for droplets with $\mu_{sph} = 0.03$ and a solid-fluid interaction strength of $s_{sf} = 0.01$, 0.02 and 0.03. The equilibrium radius of the droplets is $R_{eq} = 5.85$.

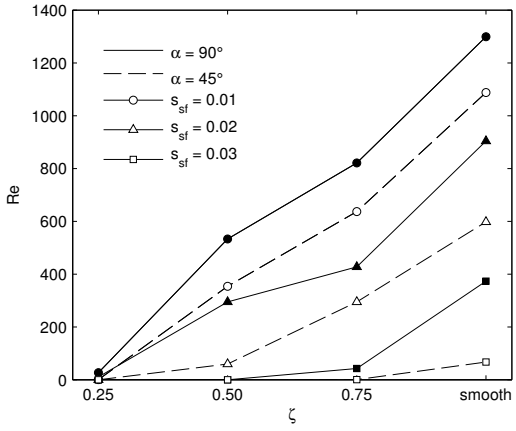

Figure 18: Reynolds numbers for three roughness coefficients, three static contact angles (110°, 80°, 60°) and two inclination angles.

[1] Evans, D.D., Rasmussen, T.C.. Unsaturated Flow and Transport Through Fractured Rock Related to High-level Waste Repositories: Final Report–phase III. Tech. Rep.; Office of Nuclear Regulatory Research; Washington; 1991.

[2] Singhal, B.B., Gupta, R.P.. Applied Hydrogeology of Fractured Rocks. Springer; 2010. ISBN 9048187982.

[3] Mclaren, R.G., Forsyth, P.A., Sudicky, E.A., Vanderkwaak, J.E., Schwartz, F.W., Kessler, J.H.. Flow and transport in fractured tuff at Yucca Mountain: numerical experiments on fast preferential flow mechanisms. J Contam Hydrol 2000;43:211–238. doi:10.1016/S0169-7722(00)00085-1.

[4] Evans, D.D., T., N.J., Rasmussen, T.C.. Flow and Transport Through Unsaturated Fractured Rock. Geoph Monog Series 2001;42:201.

[5] Mualem, Y.. A new model for predicting the hydraulic conductivity of unsaturated porous media. Water Resour Res 1976;12(3):513–522. doi:10.1029/2010WR009092.

[6] van Genuchten, M.T.. A Closed-form Equation for Predicting the Hydraulic Conductivity of Unsaturated Soils. Soil Sci Soc Am J 1980;44(5):892–898. doi:10.1029/97WR00473.

[7] Tokunaga, T.K., Wan, J.. Water film flow along fracture surfaces of porous rock. Water Resour Res 1997;33(6):1287. doi:10.1029/97WR00473.

[8] Tokunaga, T.K., Wan, J., Sutton, S.R.. Transient film flow on rough fracture surfaces. Water Resour Res 2000;36(7):1737–1746. doi: 10.1029/2000WR900079.

[9] Doe, T.. What do drops do? Surface wetting and network geometry effects on vadose-zone fracture flow. In: Conceptual models of flow and transport in the fractured vadose zone; chap. 8. Washington D.C.: National Academy Press; 2001, p. 243–270.

[10] Dragila, M.I., Weisbrod, N.. Parameters affecting maximum fluid transport in large aperture fractures. Adv Water Resour 2003;26:1219–1228. doi:10.1016/j.advwatres.2003.09.002.

[11] Su, G.W., Geller, J.T., Pruess, K., Hunt, J.R.. Solute transport along preferential flow paths in unsaturated fractures. Water Resour Res 2001;37(10):2481–2491. doi:10.1029/2000WR000093.

[12] Dragila, M.I., Weisbrod, N.. Flow in Menisci Corners of Capillary Rivulets. Vadose Zone J 2004;3:1439–1442. doi:10.2113/3.4.1439.

[13] Dragila, M.I., Weisbrod, N.. Fluid motion through an unsaturated fracture junction. Water Resour Res 2004;40:1–11. doi: 10.1029/2003WR002588.

[14] Su, G.W., Geller, J.T., Hunt, J.R., Pruess, K.. Small-Scale Features of Gravity-Driven Flow in Unsaturated Fractures. Vadose Zone J 2004;3(2):592–601. doi:10.2113/3.2.592.

[15] Germann, P.F., Helbling, A., Vadilonga, T.. Rivulet Approach to

Rates of Preferential Infiltration. Vadose Zone J 2007;6(2):207–220. doi: 10.2136/vzj2006.0115.

[16] Ghezzehei, T.A.. Constraints for flow regimes on smooth fracture surfaces. Water Resour Res 2004;40:1–14. doi:10.1029/ 2004WR003164.

[17] Podgorski, T., Flesselles, J.M., Limat, L.. Corners, Cusps, and Pearls in Running Drops. Phys Rev Lett 2001;87(3):036102. doi: 10.1103/PhysRevLett.87.036102.

[18] Hirt, C., Nichols, B.. Volume of Fluid (VOF) Method for the Dynamics of Free Boundaries. J Comput Phys 1981;39:201–225. doi:10.1016/0021-9991(81)90145-5.

[19] Huang, H., Meakin, P.. Three-dimensional simulation of liquid drop dynamics within unsaturated vertical Hele-Shaw cells. Water Resour Res 2008;44(3):W03411. doi:10.1029/2007WR006158.

[20] Lucy, L.B.. A numerical approach to the testing of the fission hypothesis. Astron J 1977;82(12):1013–1024.

[21] Gingold, R.A., Monaghan, J.J.. Smoothed particle hydrodynamics: theory and application to non-spherical stars. Mon Not R Astron Soc 1977;181:375–389.

[22] Hoover, W.G., Pierce, T.G., Hoover, C.G., Shugart, J.O., Stein, C.M., Edwards, A.L.. Molecular Dynamics , Smoothed-Particle Applied Mechanics , and Irreversibility. Comput Math Appl 1994;28(10):155–174. doi:10.1016/0898-1221(94)00191-X.

[23] Tartakovsky, A.M., Meakin, P.. Modeling of surface tension and contact angles with smoothed particle hydrodynamics. Phys Rev E 2005;72:026301. doi:10.1103/PhysRevE.72.026301.

[24] Meakin, P., Tartakovsky, A.M.. Modeling and simulation of pore-scale multiphase fluid flow and reactive transport in fractured and porous media. Rev Geophys 2009;(2008):1–47. doi:10.1029/2008RG000263.

[25] Holmes, D., Williams, J., Tilke, P., Leonardi, C.. Characterizing flow in oil reservoir rock using SPH: Absolute permeability. Int J Numer Anal Met 2000;61(7):1–22.

[26] Tartakovsky, A.M., Meakin, P.. Pore scale modeling of immiscible and miscible fluid flows using smoothed particle hydrodynamics. Adv Water Resour 2006;29(10):1464–1478. doi:10.1016/j.advwatres.2005.11.014.

[27] Tartakovsky, A.M., Ferris, K.F., Meakin, P.. Lagrangian particle model for multiphase flows. Comput Phys Commun 2009;180(10):1874–1881. doi:10.1016/j.cpc.2009.06.002.

[28] Holmes, D., Williams, J., Tilke, P.. Smooth particle hydrodynamics simulations of low Reynolds number flows through porous media. Int J Numer Anal Met 2011;35:419–437. doi:10.1002/nag.898.

[29] Tartakovsky, A.M., Meakin, P.. Simulation of Unsaturated Flow in Complex Fractures Using Smoothed Particle Hydrodynamics. Vadose Zone J 2005;4(3):848–855. doi:10.2136/vzj2004.0178.

[30] Tartakovsky, A.M., Ward, A.L., Meakin, P.. Pore-scale simulations of

drainage of heterogeneous and anisotropic porous media. Phys Fluids 2007;19(10):103301. doi:10.1063/1.2772529.

[31] ElSherbini, A.I., Jacobi, A.M.. Liquid drops on vertical and inclined surfaces; I. An experimental study of drop geometry. J Colloid Interf Sci 2004;273(2):556–65. doi:10.1016/j.jcis.2003.12.067.

[32] ElSherbini, A.I., Jacobi, A.M.. Retention forces and contact angles for critical liquid drops on non-horizontal surfaces. J Colloid Interf Sci 2006;299(2):841–9. doi:10.1016/j.jcis.2006.02.018.

[33] Monaghan, J.J.. Why particle methods work. SIAM J Sci Stat Comp 1982;3(4):422 – 433. doi:10.1137/0903027.

[34] Tartakovsky, A.M., Meakin, P.. A smoothed particle hydrodynamics model for miscible flow in three-dimensional fractures and the two-dimensional Rayleigh-Taylor instability. J Comput Phys 2005;207:610–624. doi:10.1016/j.jcp.2005.02.001.

[35] Huh, C., Scriven, L.. Hydrodynamic model of steady movement of a solid/liquid/fluid contact line. J Colloid Interf Sci 1971;35(1):85–101. doi:10.1016/0021-9797(71)90188-3.

[36] Tanner, L.. The spreading of silicone oil drops on horizontal surfaces. J Phys D Appl Phys 1979;12(9):1473–1485. doi:doi:10.1088/0022-3727/12/9/009.

[37] de Gennes, P.. Wetting: statics and dynamics. Rev Mod Phys 1985;57(3):827–863. doi:10.1103/RevModPhys.57.827.

[38] Gingold, R.A., Monaghan, J.J.. Kernel estimates as a basis for general particle methods in hydrodynamics. J Comput Phys 1982;46(3):429–453. doi:10.1016/0021-9991(82)90025-0.

[39] Morris, J.P.. Modeling Low Reynolds Number Incompressible Flows Using SPH. J Comput Phys 1997;136(1):214–226. doi:10.1006/jcph.1997.5776.

[40] Liu, M., Meakin, P., Huang, H.. Dissipative particle dynamics with attractive and repulsive particle-particle interactions. Phys Fluids 2006;18(1):017101. doi:10.1063/1.2163366.

[41] Brackbill, J., Kothe, D., Zemach, C.. A continuum method for modeling surface tension. J Comput Phys 1992;100(2):335–354. doi:10.1016/0021-9991(92)90240-Y.

[42] Allen, M., Tildesley, D.. Computer Simulation of Liquids. Clarendon Press, Oxford; 1989. ISBN 0198556454.

[43] Kwok, D.Y., Gietzelt, T., Grundke, K., Jacobasch, H.J., Neumann, a.W.. Contact Angle Measurements and Contact Angle Interpretation. 1. Contact Angle Measurements by Axisymmetric Drop Shape Analysis and a Goniometer Sessile Drop Technique. Langmuir 1997;13(10):2880–2894. doi:10.1021/la9608021.

[44] Bikerman, J.. Sliding of drops from surfaces of different roughnesses. J Colloid Sci 1950;5(4):349–359. doi:10.1016/0095-8522(50)90059-6.

[45] Furmidge, C.. Studies at phase interfaces. I. The sliding of liquid

drops on solid surfaces and a theory for spray retention. J Colloid Sci 1962;17(4):309–324. doi:10.1016/0095-8522(62)90011-9.

[46] Dussan V., E.B., Chow, R.T.P.. On the ability of drops or bubbles to stick to non-horizontal surfaces of solids. J Fluid Mech 1983;137:1–29. doi:10.1017/S002211208300227X.

[47] Grand, N., Daerr, A., Limat, L.. Shape and motion of drops sliding down an inclined plane. J Fluid Mech 2005;541:293. doi:10.1017/S0022112005006105.

[48] Huang, J.J., Shu, C., Chew, Y.T.. Lattice Boltzmann study of droplet motion inside a grooved channel. Phys Fluids 2009;21:1–11. doi:10.1063/1.3077800.

[49] Mognetti, B., Kusumaatmaja, H., Yeomans, J.. Drop dynamics on hydrophobic and superhydrophobic surfaces. Faraday Discuss 2010;146:153–165. doi:10.1039/b926373j.

[50] Jiang, T., Ouyang, J., Yang, B., Ren, J.. The SPH method for simulating a viscoelastic drop impact and spreading on an inclined plate. Comput Mech 2010;45(6):573–583. doi:10.1007/s00466-010-0471-7.

[51] Macdougall, G., Ockrent, C.. Surface Energy Relations in Liquid/Solid Systems. I. The Adhesion of Liquids to Solids and a New Method of Determining the Surface Tension of Liquids. Proc R Soc Lon Ser-A 1942;180:151. doi:10.1098/rspa.1942.0031.

[52] Tsukada, T., Hozawa, M., Imaishi, N., Fujikawa, K.. Static drop

formation on an inclined flat plate. J Chem Eng Jpn 1982;15:412–426. doi:10.1252/jcej.19.537.

[53] Or, D., Tuller, M.. Flow in unsaturated fractured porous media: Hydraulic conductivity of rough surfaces. Water Resour Res 2000;36(5):1165–1177. doi:10.1029/2000WR900020.

[54] Lebeau, M., Konrad, J.M.. A new capillary and thin film flow model for predicting the hydraulic conductivity of unsaturated porous media. Water Resour Res 2010;46(12):1–15. doi:10.1029/2010WR009092.

[55] Su, G.W., Geller, J.T., Pruess, K., Wen, F.. Experimental studies of water seepage and intermittent flow in unsaturated, rough-walled fractures. Water Resour Res 1999;35(4):1019. doi:10.1029/1998WR900127.

[56] Sobolev, V., Churaev, N., Velarde, M., Zorin, Z.. Surface Tension and Dynamic Contact Angle of Water in Thin Quartz Capillaries. J Colloid Interf Sci 2000;222(1):51–54. doi:10.1006/jcis.1999.6597.

[57] Tokunaga, T.K., Wan, J.. Surface-zone flow along unsaturated rock fractures. Water Resour Res 2001;37(2):287. doi:10.1029/2000WR900242.

[58] Mandelbrot, B.. The fractal geometry of nature. 1982.

[59] Bouchaud, E., Lapasset, G., Planes, J.. Fractal dimension of fractured surfaces: a universal value? Europhys Lett 1990;73(13):73–79. doi:10.1209/0295-5075/13/1/013.

[60] Bouchaud, E.. Scaling properties of cracks. J Phys-Condens Mat 1997;9(21):4319–4344. doi:10.1088/0953-8984/9/21/002.

[61] Ponson, L., Bonamy, D., Bouchaud, E.. Two-Dimensional Scaling Properties of Experimental Fracture Surfaces. Phys Rev Lett 2006;96(3):035506. doi:10.1103/PhysRevLett.96.035506.

[62] Marmur, A.. The Lotus Effect : Superhydrophobicity and Metastability. Langmuir 2004;(20):3517–3519. doi:10.1021/la036369u.

[63] Cassie, A.. Contact angles. Discuss Faraday Soc 1948;3:11–16. doi:10.1039/df9480300011.

[64] Monaghan, J.J.. Smoothed particle hydrodynamics. Rep Prog Phys 2005;68:1703–1759. doi:10.1088/0034-4885/68/8/R01.